

IDGCP: Image Dehazing Based on Gamma Correction Prior

Mingye Ju, Can Ding, *Member, IEEE*, Y. Jay Guo, *Fellow, IEEE*,
and Dengyin Zhang, *Member, IEEE*

Abstract—This paper introduces a novel and effective image prior, i.e., gamma correction prior (GCP), which leads to an efficient image dehazing method, i.e., IDGCP. A step-by-step procedure of the proposed IDGCP is as follows. First, an input hazy image is preprocessed by the proposed GCP, resulting in a homogeneous virtual transformation of the hazy image. Then, from the original input hazy image and its virtual transformation, the depth ratio is extracted based on atmospheric scattering theory. Finally, a “global-wise” strategy and a vision indicator are employed to recover the scene albedo, thus restoring the hazy image. Unlike other image dehazing methods, IDGCP is based on the “global-wise” strategy, and it only needs to determine one unknown constant without any refining process to attain a high-quality restoration, thereby leading to significantly reduced processing time and computation cost. Each step of IDGCP is tested experimentally to validate its robustness. Moreover, a series of experiments are conducted on a number of challenging images with IDGCP and other state-of-the-art technologies, demonstrating the superiority of IDGCP over the others in terms of restoration quality and implementation efficiency.

Index Terms—Atmospheric scattering theory, gamma correction prior (GCP), global-wise strategy, haze removal, processing time, vision indicator.

I. INTRODUCTION

HIGH quality images with rich information are crucial for computer vision applications, such as object detection [1], aerial imagery [2], and image classification [3]. However, low visibility due to hazy weather condition or other factitious reasons can significantly deteriorate the quality of images captured by cameras. These low-quality images can seriously impair the proper functioning of a computer vision system that needs high-quality inputs. Image dehazing is the key technology to recover hazy images and remove adverse visual effects.

Traditionally, image haze removal was realized by enhancing the global contrast or local contrast of blurred images

Manuscript submitted April 2, 2019; revised September 7, 2019; revised November 19, 2019. This work was supported by National Natural Science Foundation of China (61902198, 61872423), Natural Science Foundation of Jiangsu Province (BK20190730), and Research Fund of Nanjing University of Posts and Telecommunications (NY219135). (Corresponding author: Dengyin Zhang and Can Ding)

M. Ju and D. Zhang are with the School of Internet of Things, Nanjing University of Posts and Telecommunications, Nanjing, 210000, China. M. Ju is also with the Global Big Data Technologies Centre (GBDTC), University of Technology Sydney (UTS), Ultimo, NSW, 2007, Australia. e-mail:(jumingye@njupt.edu.cn, mingye.ju@student.uts.edu.au)

C. Ding and Y. Jay Guo are with the Global Big Data Technologies Centre (GBDTC), University of Technology Sydney (UTS), Ultimo, NSW, 2007, Australia. e-mail:(can.ding.1989@gmail.com)

[4]–[8]. This is the simplest and most intuitive way to recall visibility. However, these methods neglect the degrading mechanism of hazy images, thereby limiting the recovery performance. To address the shortcomings of these traditional methods, a fusion-wise strategy was recommended in [9], [10]. This fusion-wise strategy first uses several traditional techniques to preprocess a hazy input image, and then blends the preprocessed results into one image by using a Laplacian pyramid representation. However, when the hazy images are dark or the haze is dense, this strategy exhibits limited dehazing performance because of the inappropriate weighting of the dark objects.

Another kind of solutions advocated in [11], [12] is capable of generating better results. These solutions are based on atmospheric scattering theory and require multiple sources or other external information. Narasimhan et al. [11] used two images taken in different atmospheric conditions and Kopf et al. [12] exploited the given geo-referenced digital terrain, to derive the depth map and the other unknown parameters that are required to recover the image. However, in reality, the requested external information is usually not available or needs high cost prerequisites, thus these methods have limited practicability in many applications.

The recently emerged image prior knowledge provides an alternative kind of solutions which leads to a series of single image haze removal algorithms. These methods can be further divided into following categories, including pixel-wise [13]–[18], patch-wise [19]–[29], scene-wise [30]–[32], and nonlocal-wise strategies [33]–[35], depending on their approaches of finding the transmission map of input images. The working mechanisms of these strategies are sketched in Figs. 1(a) to 1(d), respectively.

As illustrated in Fig. 1(a), in the pixel-wise strategy, the transmission map is obtained by acquiring the minimum channel information from each pixel in an image. The main advantage of the pixel-wise strategy is its high implementation efficiency, but a single pixel does not have sufficient information to determine the transmission. Meanwhile, the transmission map computed via pixel-wise strategy is bound to contain a lot of unreasonable texture details, thus subsequent blurring procedure is required. Typically, Tarel and Hautiere [13] estimated the atmospheric veil associated with minimum channel to achieve haze removal. This method can recover most of the scenic details. However, the over-enhancement problem might exist in mist scenes, and a small amount of mist might still remain in the discontinuous areas due to the employed mean filter (MF).

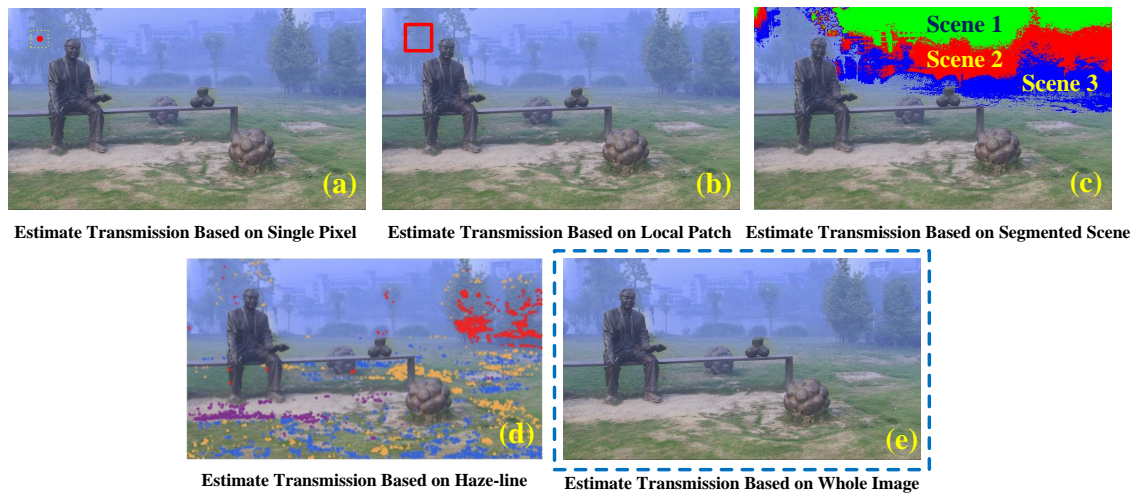


Fig. 1. Working mechanisms of different image dehazing strategies for estimating transmission map. (a) Pixel-wise strategy. (b) Patch-wise strategy. (c) Scene-wise strategy (region with same color represents an independent scene). (d) Nonlocal-wise strategy (pixels with same color represent the clustered haze-line). (e) Global-wise strategy.

The patch-wise strategy shown in Fig. 1(b) determines the transmission map by extracting local information from each patch. This strategy can overcome the limitation of pixel-wise strategy to some extent since a patch has richer information than a pixel. However, the computed transmission map still has a large number of estimation errors, and the complex edge-guided tools are needed to eliminate the halo artifacts introduced by this strategy. For example, He¹ et al. [19] proposed the patch-based dark channel prior (DCP) to directly detect the rough haze thickness of a hazy image, and then the realistic haze-free images can be obtained by refining the initial transmission map using soft matting (SM) [37]. Unfortunately, DCP approach cannot well handle the regions where the brightness of scene targets is inherently similar to the atmospheric light. In [20], Bui and Kim developed a novel single image dehazing method based on the color ellipsoid prior. This method can generate the transmission map by maximizing the contrast of recovered pixels while avoiding the over-saturation. However, this method misjudges the close-range area with high-bright as dense haze, and the fuzzy segmentation process used for suppressing halo artifacts would reduce the dehazing efficiency.

To attain more information for transmission map estimation, more robust scene-wise strategy was advocated in [30]–[32]. The scene-wise strategy utilizes a cluster operator to segregate the input images, as shown in Fig. 1(c). The core idea is to expand the transmission estimation range from patch to scene, thus the restoration performance can be improved for most cases. However, clustering technique used in these methods lacks the ability to accurately segment all scenes in an input image, which introduces transmission estimation errors in depth discontinuities. Although guided total variation model (GTV) [30] and guided filter (GF) [36] were introduced to repair such discontinuity interference, scene-wise strategy based methods still suffer from adverse visual effects in the scene depth with vague classification features.

Nonlocal-wise strategy is based on a key assumption that

a hazy image must contain approximated colors [33], [34] or repeated patches [35]. Takeing color-based nonlocal-wise method [34] shown in Fig. 1(d) as an example, the first step of this method is to recognize each set of distinct colors termed as haze-line via spherical coordinates. Then, by combining these haze-lines and bound regularization (BR), the transmission map can be directly estimated according to atmospheric scattering theory. This method exhibits a very promising performance. However, as the hazy level increases, the classification accuracy decreases, thus causing the haze-line method lose its efficacy in addressing heavy haze. Another drawback of this strategy is that it also fails in scenes where the airlight is significantly brighter than the scenes.

Recently, deep learning theory has attracted significant interests and has been successfully used in image dehazing [26]–[29]. Powerful image dehazing systems can be obtained after training with numerous samples. For example, a trainable end-to-end system developed in [26] employs convolutional neural networks (CNN) to estimate scene transmission by merging some existing image priors. In subsequence, a multi-scale CNN (MSCNN) to learn effective features for determining the transmission was proposed in [27]. In [28], a dehazing model built with the CNN, called All-in-One Dehazing Network (AOD-Net) was proposed. The main advantage of AOD-Net is that it can directly obtain the haze-free result from a single hazy image through a light-weight CNN. Actually, this strategy is also based on the processing of local patches in single images, thus it can also be regarded as the “advanced” patch-wise strategy illustrated in Fig. 1(b). Although these learning-wise strategy based deep dehazing methods are capable of merging or learning the haze-relevant features to relieve the limitations of the patch-wise strategy, they also have some drawbacks, e.g., unable to deal with dense haze, needs numerous training samples.

Overall, due to the similarity of spatial structure, these existing dehazing techniques that deploy the strategies of pixel-wise, patch-wise, scene-wise, nonlocal-wise, and learning-



Fig. 2. Visual observation of hazy images \mathbf{I} (top row) and the inverted results accordingly ($1 - \mathbf{I}$) (bottom row).

wise all require redundant computation, and the transmission refining tools (MF, SM, GTV, GF, BR, CNN, and MSCNN) employed by the strategies mentioned above lead to additional processing times, thus degrading the execution efficiency of haze removal. Moreover, although the aforementioned priors all have some advantages, they are not able to handle all practical situations, which might result in vulnerable images and visual inconsistency.

In this paper, a novel dehazing method named IDGCP employing a global-wise strategy is proposed. As schematically illustrated in Fig. 1(e), when acquiring the transmission information, the input image is considered as a whole block rather than dividing the image into several pixels, patches, scenes, or approximate objects. A gamma correction prior (GCP) for single image dehazing is proposed. Using GCP, the input image is transformed into a virtual image. Based on the atmospheric scattering model (ASM) and by combining the obtained virtual image and the input hazy image, the depth ratio information can be determined for image dehazing. Different from existing techniques, IDGCP only estimates one unknown constant by extracting the depth ratio from the two images (original input image and virtual image), which leads to a significantly reduced processing time. Moreover, IDGCP also achieves a better restoration of object colors and target details.

The remainder of the paper is organized as follows. Following introduction, Section II revisits the atmospheric scattering model and theory. The models of GCP and IDGCP are developed in Sections III and IV, respectively. Section V evaluates the performance of IDGCP by conducting a series of comparisons between IDGCP and state-of-the-art techniques. Finally, Section VI concludes the paper.

II. ATMOSPHERIC SCATTERING MODEL (ASM)

The image dehazing in this work is based on the ASM proposed by Narasimhan and Nayar [11] to describe the formation of hazy images. This model is widely used in computer vision and computer graphics and can be expressed as

$$\mathbf{I}(x, y) = \mathbf{A} \cdot \rho(x, y) \cdot t(x, y) + \mathbf{A} \cdot (1 - t(x, y)), \quad (1)$$

where \mathbf{I} represents the observed hazy image, \mathbf{A} is the global atmospheric light, ρ is scene albedo or the expected haze-free

image, and t is the medium transmission. When the atmospheric particle distribution is homogeneous, i.e., the atmospheric medium is evenly distributed throughout the whole image, the transmission t can be obtained as

$$t(x, y) = e^{-\beta \cdot d(x, y)}, \quad (2)$$

where d is the distance between the target scene and the camera (or scene depth), β is the scattering coefficient assumed to be constant. In this model, the first term on the right side of Eq. 1 is used to describe the direct impact of scene reflection light $\mathbf{A} \cdot \rho$ from suspended particles. This term is named as **Direct Attenuation** which decays exponentially with the scene depth d . The second term called **Airlight**, on the contrary, increases with the scene depth d .

It is commonly known that single image haze removal is a highly under-constrained problem since the number of unknowns is much greater than the number of available equations. Although some works have been done to address this problem, there are still two key issues remain unsolved. The first one is that the proposed image priors or assumptions cannot work well in all cases as illustrated in Section I. The other issue is the long processing time attributed to the involved refining tools and redundant computations.

The next section will introduce a robust gamma correction prior (GCP), which is one of the two key contributions of this work. It is able to get a virtual misty result under homogeneous atmosphere from the original input. Based on the obtained virtual image and the original image, the depth ratio information can be directly extracted.

III. GAMMA CORRECTION PRIOR (GCP)

A. Motivation

In [38], gamma correction (GC) strategy was proposed by Liu et al. to preprocess hazy input image. Despite the fact that this valuable strategy can improve the overall brightness of images, it suffers from a problem that the haze cover in hazy image is also processed by GC without considering the scene depth information [17]. In specific, the preprocess can be expressed by

$$\mathbf{I}_p^c = (\mathbf{I}^c)^\Gamma, \quad (3)$$

where $c \in \{\text{R, G, B}\}$ is the color channel index, \mathbf{I}^c is the color channel of the input \mathbf{I} , $0 < \Gamma < 1$ is the correction factor,

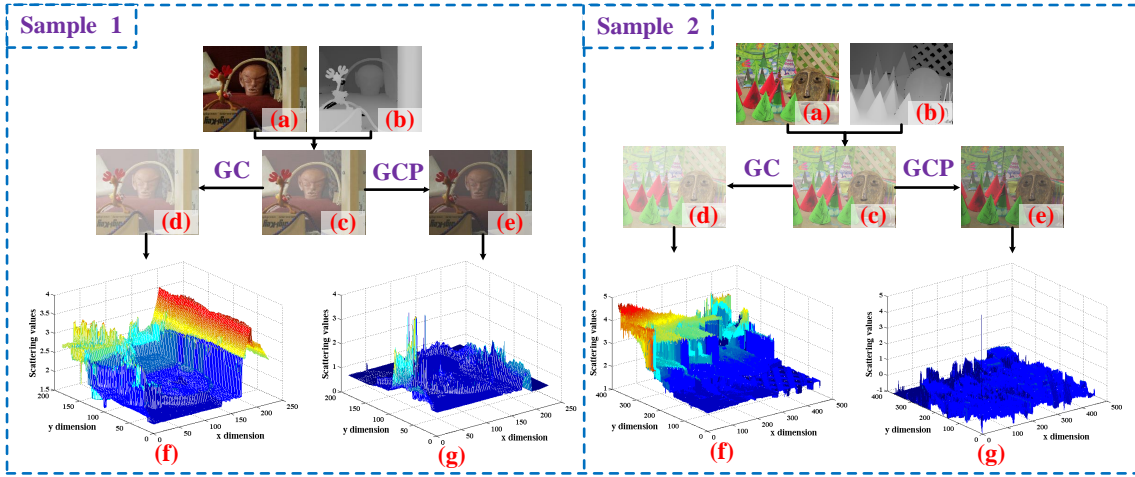


Fig. 3. Illustration of the GC and GCP processes on two example images. (a) Ground truth images. (b) Depth maps. (c) Synthesized images via SMP with $A^c = 1$ and $\beta = 1$. (d) Obtained virtual results using GC with $\Gamma = 0.5$. (e) Obtained virtual results using GCP with $\Gamma = 0.5$. (f) The scattering values of all pixels in (d). (g) The scattering values of all pixels in (e).

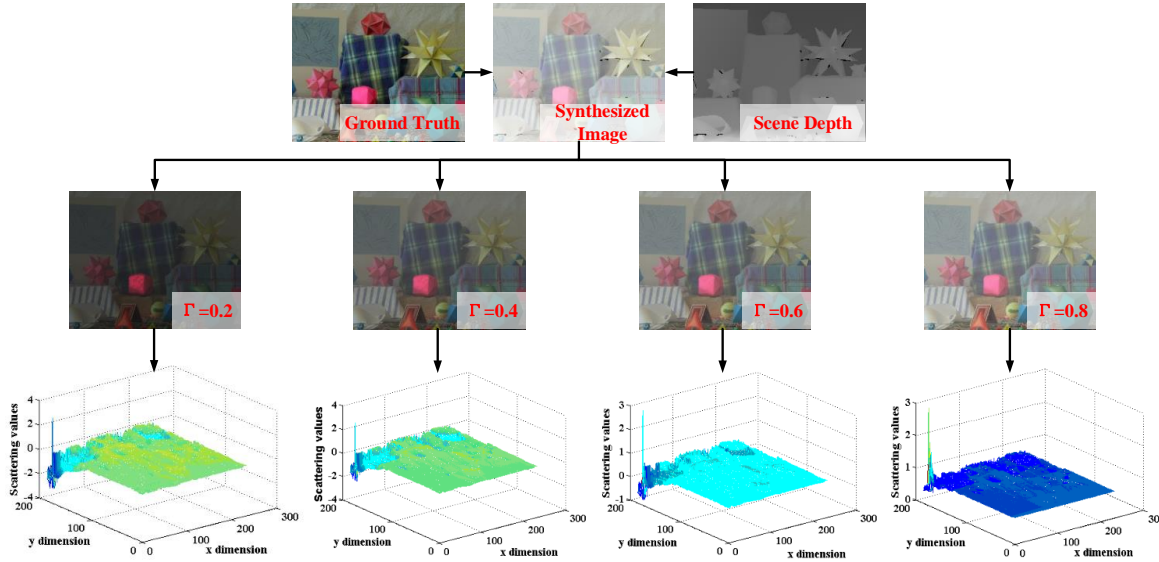


Fig. 4. Robustness evaluation of GCP with different values of Γ . **Top row:** Sample image. **Middle row:** Virtual results using GCP with different Γ . **Bottom row:** Corresponding scattering coefficient values for all pixels.

and I_p is the preprocessed result. Assuming that I_p meets the premise of using ASM, Eq. 3 can be transformed into

$$A_p^c \cdot ((\rho^c(x, y) - 1) \cdot e^{-\beta_p \cdot d(x, y)} + 1) \\ = (A^c)^\Gamma \cdot ((\rho^c(x, y) - 1) \cdot e^{-\beta \cdot d(x, y)} + 1)^\Gamma, \quad (4)$$

where β_p and A_p^c are the scattering coefficient and atmospheric light, respectively, of the color channel I_p^c . Obviously, the location of atmospheric light in a given image should remain the same before and after the GC preprocess. Therefore, we let $A_p^c = (A^c)^\Gamma$ and subtract $(A^c)^\Gamma$ from each side of Eq. 4, which yields

$$(\rho^c(x, y) - 1) \cdot e^{-\beta_p \cdot d(x, y)} \\ = \{(\rho^c(x, y) - 1) \cdot e^{-\beta \cdot d(x, y)} + 1\}^\Gamma - 1. \quad (5)$$

Considering the fact that $(\rho^c(x, y) - 1) \cdot e^{-\beta \cdot d(x, y)}$ is close to 0 in general, especially for dense hazy regions, Eq. 5 is then simplified according to the equivalent infinitesimal theorem.

$$(\rho^c(x, y) - 1) \cdot (e^{-\beta_p \cdot d(x, y)} - \Gamma \cdot e^{-\beta \cdot d(x, y)}) \approx 0 \\ \Rightarrow \beta_p \approx \beta - \frac{\ln(\Gamma)}{d}. \quad (6)$$

Since the correction constant Γ is a constant and $[\ln(\Gamma) < 0]$, the obtained scattering coefficient of the preprocessed image β_p decreases with scene depth d . This indicates a fact that the GC preprocess turns the homogeneous input image into an inhomogeneous virtual output image, i.e., the spatial distribution of the atmospheric medium varies throughout the image. In close-range regions with small d , β_p is higher, which leads to a brighter result than the homogenous case. In contrast, in long-range regions, the preprocessed results will appear to

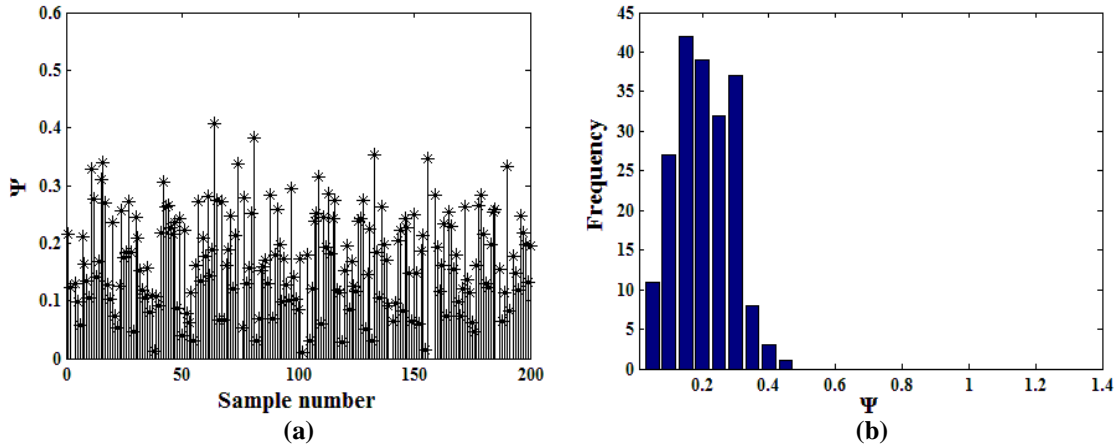


Fig. 5. Statistics of the index Ψ . (a) Values of Ψ over 200 test samples. (b) Statistical histogram corresponding to the left statistics.

be darker. This problem increases the complexity of the haze removal. Even with a known scene depth, one would need to estimate the spatially variable scattering values to achieve a high performance image dehazing.

B. GCP model

In this paper, a modified preprocessing method called gamma correction prior (GCP) is proposed. The main difference between GC [38] and GCP is the fact that their outputs are inhomogeneous and homogeneous, respectively. The proposed GCP model is described as

$$\mathbf{I}_s^c = 1 - (1 - \mathbf{I}^c)^\Gamma, \quad (7)$$

where \mathbf{I}_s is the virtual result. In this process, the hazy image \mathbf{I} get inverted first into $1 - \mathbf{I}$. Then it is processed by the GC and inverted back to get the virtual result. The inverse strategy was firstly proposed in [39] and used in image enhancement [40], [41] based on an observation that the inverted low-light images look similar to hazy images. In this work, we made a further assumption that the inverted hazy image $1 - \mathbf{I}$ is also visually very similar to low-light images (see Fig. 2). By inverting the image, the brighter regions and the darker regions are swapped. Since the inverse strategy and the GC have adverse effects on the scattering coefficient β with different scene depth, the GCP has a potential to compensate the nonlinearity in GC and stabilize the scattering coefficient β .

A large amount of experiments were conducted to investigate the GCP's ability to stabilize β . In the experiments, the input \mathbf{I} in Eq. 1 was replaced by \mathbf{I}_s to compute the scattering values β_s for each pixel in \mathbf{I}_s . Therefore, we have

$$\beta_s(x, y) = -\log\left(\frac{(1 - (1 - \mathbf{I}^c(x, y))^\Gamma - \mathbf{A}_s^c)}{\mathbf{A}_s^c \cdot (\rho^c(x, y) - 1)}\right)/d, \quad (8)$$

where \mathbf{A}_s^c is the atmospheric light of the virtual results \mathbf{I}_s^c . There are various methods [14], [19], [42], [43] can be used to locate the atmospheric light. With the overall consideration of performance and efficiency, the quad-tree subdivision method proposed in [14] was selected since it can accurately locate

the atmospheric light from the most haze-opaque region by combining the average grays and gradients based assessment criteria and quad-tree subdivision. Here we remark that one can also use other methods to estimate the atmospheric light depending on the main concerns. As illustrated in Eq. 8, the ground depth information (d) is required to calculate β_s . However, it is very hard to get the depth information from real world images. Therefore, in this work, the image samples were synthesized using the depth maps and ground truth images in Middlebury Stereo Datasets [44]–[46] according to Eq. 1. This synthesis procedure is named as SMP in the following sections for the ease of clarify.

Fig. 3 shows the simulated results of two samples using GC and GCP with $\Gamma = 0.5$, as well as the computed scattering coefficients. According to Fig. 3(f) and 3(g), GCP demonstrates a significantly enhanced ability of stabilizing the scattering coefficients compared to that of GC. Fig. 4 illustrates the GCP process on a third sample with different Γ values. It is observed that scattering coefficients of the outputs of the GCP always have a high level of stability which is independent to Γ values. Moreover, to quantitatively evaluate the robustness of GCP, a statistic indicator is defined as

$$\Psi = \sqrt{\frac{1}{|\Omega|} \sum_{(x,y) \in \Omega} (\beta_s(x, y) - \bar{\beta}_s)^2}, \quad (9)$$

where $\bar{\beta}_s$ is the average value of β_s , Ω and $|\Omega|$ are the image index set and image resolution, respectively. Generally, the smaller the value of Ψ is, the more stable the scattering coefficients, which indicates that the GCP is more reliable. The calculated Ψ values of 200 different samples processed by GCP are shown in Fig. 5(a), and the statistic histogram is shown in Fig. 5(b). It is observed that 90% of the samples have small Ψ values ≤ 0.3 , which validates the reliability of the proposed GCP. It can be summarized that the proposed GCP process overcomes the limitation of the GC since the homogeneity of input images is well maintained in the output images.

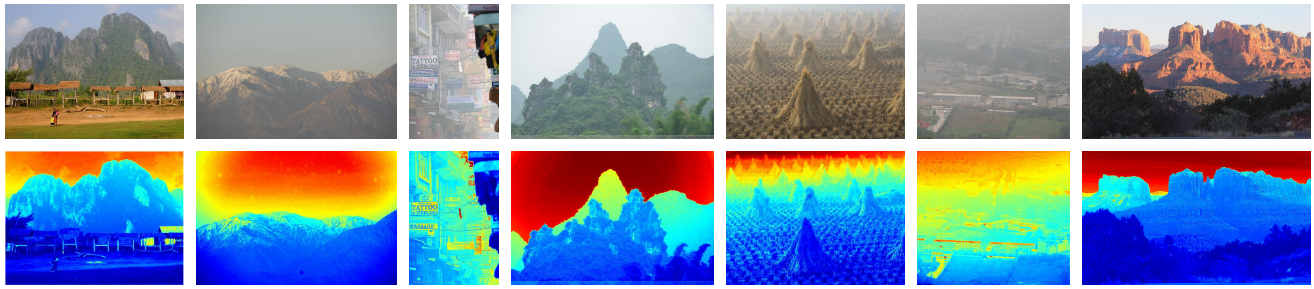


Fig. 6. Example images and the estimated depth ratio maps. **Top row:** Input hazy images. **Bottom row:** Scene depth ratio maps obtained using Eq. 12.

It should be noted that, although the proposed GCP is a modification of GC, they have different targets. GC can and is only used to increase the contrast of a hazy image, whereas GCP allows us to obtain a virtual misty image from a single hazy image. Combining the input hazy image with the obtained virtual image, single image dehazing problem can be converted into multiple image haze removal. The main benefit is to ease the uncertainty of depth information, which significantly facilitates the subsequent image dehazing process based on ASM.

IV. IMAGE DEHAZING BASED ON GCP (IDGCP)

In this section, based on the ASM proposed in [11] and the GCP described in the previous section, a fast image dehazing method called IDGCP is developed based on a global-wise strategy. The proposed method can extract the depth ratio efficiently by fully leveraging the latent relation of the image structure, thereby attaining haze-free results. Only two major modules are utilized in IDGCP, i.e., the depth ratio extraction module and the image recovery module.

A. Extracting Depth Ratio

The fundamental idea of IDGCP is to mine the depth structure information from the two hazy images: one is the hazy input and the other is the virtual hazy image obtained from GCP. The first step is to utilize GCP to get the virtual image \mathbf{I}_s from the original input \mathbf{I} . Then, two imaging equations for \mathbf{I}_s and \mathbf{I} are obtained based on the ASM and the structure invariance principle described in [11].

$$\begin{aligned} \mathbf{I}^c(x, y) &= \mathbf{A}^c \cdot \rho(x, y) \cdot e^{-\beta \cdot d(x, y)} + \mathbf{A}^c \cdot (1 - e^{-\beta \cdot d(x, y)}) \\ \mathbf{I}_s^c(x, y) &= \mathbf{A}_s^c \cdot \rho(x, y) \cdot e^{-\beta_s \cdot d(x, y)} + \mathbf{A}_s^c \cdot (1 - e^{-\beta_s \cdot d(x, y)}). \end{aligned} \quad (10)$$

By solving this equation set, we get

$$d = \frac{-\ln \frac{\max(\mathbf{A}^c - \mathbf{I}^c, \epsilon_1)}{\max(\mathbf{A}_s^c - \mathbf{I}_s^c, \epsilon_2)}}{\beta - \beta_s} - \ln \frac{\mathbf{A}_s^c}{\mathbf{A}^c}, \quad (11)$$

where ϵ_1 and ϵ_2 are very small positive constants, ϵ_1 is introduced to avoid the numerator to exceed the function definition field, and ϵ_2 is introduced to make sure the denominator is not zero. It is further assumed that the weather condition does not change spatially, thus we have

$$d = \frac{1}{\beta - \beta_s} \cdot d_0 \propto d_0 = -\ln \frac{\max(\mathbf{A}^c - \mathbf{I}^c, \epsilon_1)}{\max(\mathbf{A}_s^c - \mathbf{I}_s^c, \epsilon_2)} - \ln \frac{\mathbf{A}_s^c}{\mathbf{A}^c}. \quad (12)$$

Note that the depth ratio d_0 is a known component since \mathbf{A}_s^c and \mathbf{A}^c can be easily obtained [14]. In this work, we selected the blue channels \mathbf{I}^B and \mathbf{I}_s^B for the calculation of d_0 . We remark that similar results can also be obtained by adopting the red channels or the green channels. Several examples of the calculated depth ratios are illustrated in Fig. 6, demonstrating a fact that the depth ratio maps obtained are sharp and exactly in consistence with our intuition.

B. Scene Albedo Recovery Using Global-wise Strategy

The dehazed image ρ^c can be obtained by substituting Eqs. 2 and 12 into Eq. 1, which yields

$$\rho^c = \frac{\mathbf{I}^c - \mathbf{A}^c}{\mathbf{A}^c \cdot e^{-\frac{\beta}{\beta - \beta_s} \cdot d_0}} + 1. \quad (13)$$

To avoid pixel overflow, it is set that $0 \leq \rho^c \leq 1$. Therefore, the final expression used for restoring the scene albedo can be rewritten as

$$\begin{aligned} \rho^c &= \text{dehaze}(\theta, \mathbf{I}^c, \mathbf{A}^c, d_0) \\ &= \min(\max(\frac{\mathbf{I}^c - \mathbf{A}^c}{\mathbf{A}^c \cdot e^{-\theta \cdot d_0}} + 1, 0), 1), \end{aligned} \quad (14)$$

where $\text{dehaze}(\cdot)$ is the abbreviation of albedo restoring function. Note that $\text{dehaze}(\cdot)$ is a function of four parameters, where \mathbf{I}^c is the input, \mathbf{A}^c can be easily calculated according to [14], d_0 is the depth ratio obtained in the previous subsection, and $\theta = \beta / (\beta - \beta_s)$ is the only unknown parameter. Determining the right value of θ to get the transmission map $t = e^{-\theta \cdot d_0}$ is critical to the dehazing quality. To estimate the value of θ with low complexity but high accuracy, a global-wise optimization function is designed as

$$\theta = \underset{c}{\operatorname{argmin}} \{ \sum f(\text{dehaze}(\theta, (\mathbf{I}^c) \downarrow^n, \mathbf{A}^c, (d_0) \downarrow^n)) \}, \quad (15)$$

where $f(\cdot)$ represents a vision indicator designed via single or multiple image prior, and \downarrow^n is a down-sampling operator with coefficient n . Numerous experiments show that generally a down-sampled image with an approximate size of $[100 \times 100]$ is good enough to determine the value of θ since it still holds the original important features of the input image. Therefore, in this work, the coefficient n is adaptively defined as

$$n = \frac{\max(w, l)}{100}, \quad (16)$$

where w and l are the width and length of input image, respectively. Considering that the goal of image dehazing

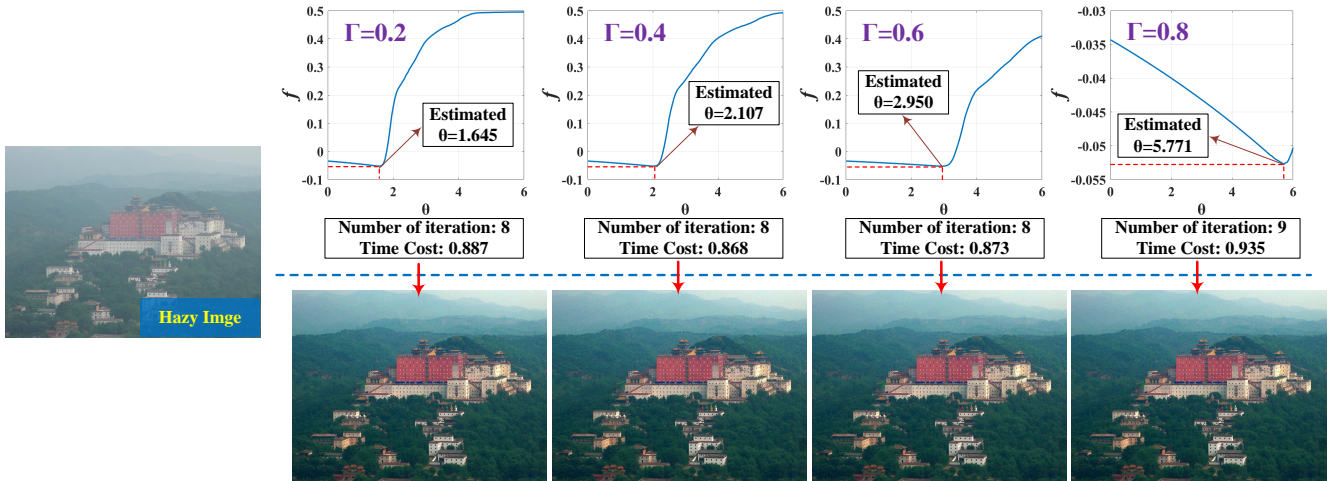


Fig. 7. IDGCP robustness evaluation of the pre-set parameter Γ on an example hazy images. **Top:** Curves of f with respect to θ using different values of Γ . **Bottom:** Results of IDGCP with different values of Γ .

is to improve the visual contrast of the degraded image while avoiding excessive loss of information [43], the vision indicator is defined as

$$f(\mathbf{In}) = - \sum_c \phi(\nabla(\mathbf{In}^c)) + \lambda \cdot \sum_c \varphi(\mathbf{In}^c), \quad (17)$$

where \mathbf{In} is the image to be evaluated, $0 \leq \lambda < 1$ is the regulation parameter, $\phi(\cdot)$ is the mean operator, and $\varphi(\cdot)$ is an operator to compute the percentage of pixels that are completely black or white. In Eq. 17, the first term ensures the image \mathbf{In} has rich texture information, and the second term is used to measure the lost information cost.

Note that Eq. 15 is a one-dimensional optimization function. In this work, Fibonacci method (FM) is adopted to solve Eq. 15 since it is able to gradually narrow the search interval for one-dimensional optimization problem until convergence condition is satisfied. In specific, the initial interval and the final interval length are defined as $[a_1, a_2]$ and ε , respectively. Once the coefficient θ is determined, the scene albedo can be directly recovered by Eq. 14. For clarity, the entire procedure of IDGCP is outlined in Algorithm 1.

Algorithm 1 IDGCP

Input: Hazy Input I

Pre-set parameters: $\epsilon_1 = \epsilon_2 = 10^{-5}$, $\lambda = 0.5$, $\Gamma = 0.5$, $[a_1, a_2] = [0, 6]$, $\varepsilon = 0.1$

Do the job:

1. Simulate the virtual image using GCP (Eq. 7).
2. Locate the atmospheric lights of the original input and the virtual image via quad-tree subdivision method [14].
3. Extract the rough depth ratio d_0 via Eq. 12.
4. Determine the constant θ via Eq. 15 with FM.
5. Restore the scene albedo via Eq. 14.

Output: Recovery result ρ

It should be pointed out that all the other dehazing methods are based on pixel-wise, patch-wise, scene-wise, nonlocal-wise, and learning-wise strategies. The proposed global-wise

strategy is the second key contribution in this paper, which enables us to attain a high-quality restoration by only determining one unknown constant.

V. PERFORMANCE EVALUATION

To demonstrate the superiority of IDGCP and to better understand where the superiority comes from, a series of experiments were conducted and comparisons were made between IDGCP and the state-of-the-art technologies. All the experiments were implemented in MATLAB2010 environment on a PC with Intel(R) Core(TM) i5-4210U CPU@ 1.70GHz 8.00 GB RAM. The parameters used in the compared dehazing methods were also optimized according to the corresponding references.

A. Initial parameter setup and robustness evaluation

As listed in Algorithm 1, there are several parameters that are initialized manually in the proposed IDGCP. They are the positive constants ϵ_1 and ϵ_2 , the correction factor Γ , the regulation constant λ , the FM's initial interval $[a_1, a_2]$, and the FM's final interval width ε . Note that the pre-set parameters illustrated in Algorithm 1 is an optimized combination which works for all kinds of hazy inputs, which can be validated by the subsequent experiments. Once their values are determined, it can be used on all images straightforwardly. In this subsection, how the values of the parameters are chosen will be described and their effects on the performance will be discussed.

The parameters ϵ_1 and ϵ_2 are introduced only to ensure that Eq. 11 remains valid. As long as they are small positive constants, their values have no effect to the final results. In this work, both ϵ_1 and ϵ_2 are set to be 10^{-5} .

The correction factor Γ is a parameter of the proposed GCP (see Eq. 7). According to the previous analysis in Section III-B and the experiment results illustrated in Fig. 4, the scattering coefficients β_s of the output virtual image always exhibit a high level of stability throughout the image, which

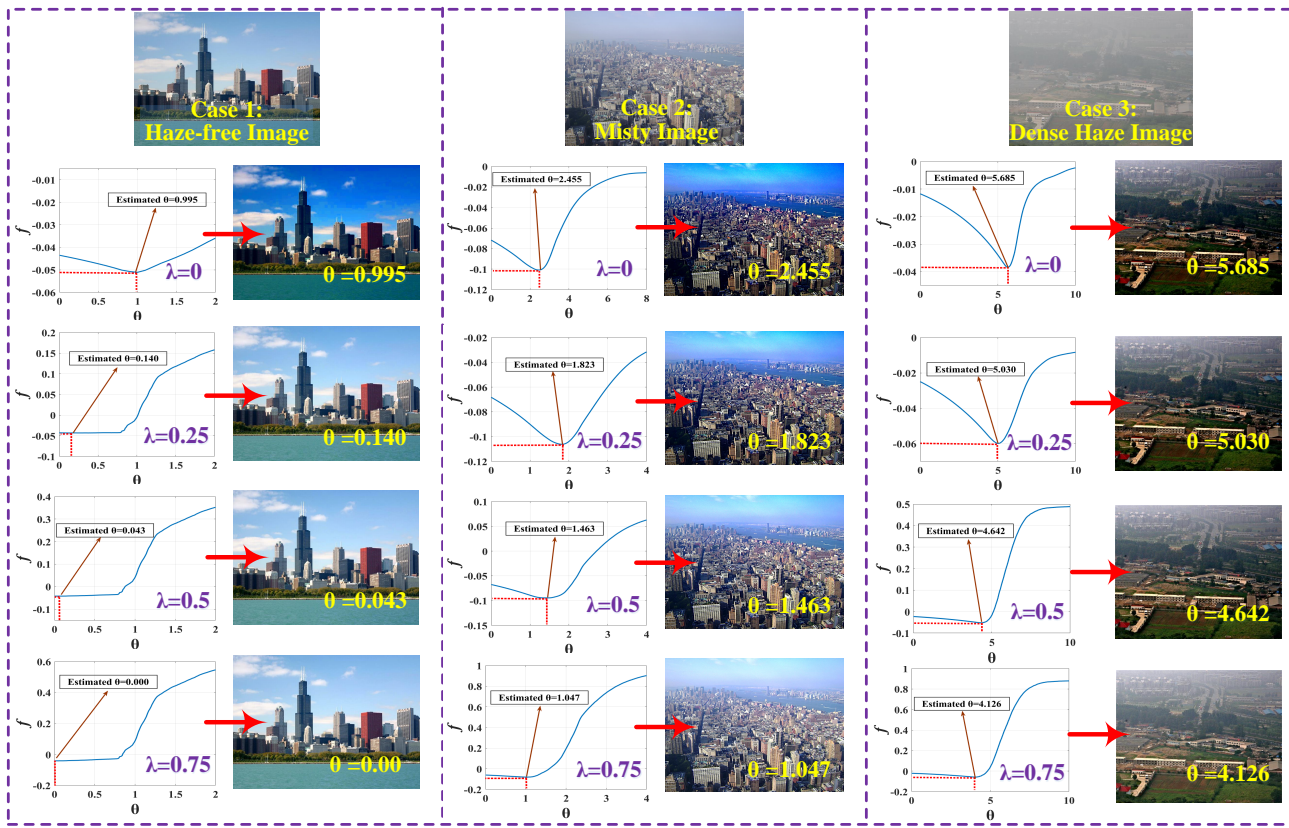


Fig. 8. IDGCP robustness evaluation of the pre-set parameter λ on three example images.

is independent to Γ values. As long as β_s can be seen as a constant, the GCP is valid. Although different values of Γ leads to different scattering coefficients β_s (see Fig. 4), it almost has no effect on the quality of the final dehazed results. Fig. 7 shows the IDGCP dehaze results on an example images with different Γ values. During the experiment, the other parameters were fixed at the values illustrated in Algorithm 1. As shown in the figure, there is barely any difference between the dehazed results when Γ has different values. However, different values of Γ lead to different values of θ (Eq. 15) and affect the processing time. The processing time is slightly different with different values of Γ because the FM used to determine the value of θ needs different numbers of iterations. For example, as shown in Fig. 7, when $\Gamma = 0.6$, the number of iteration to find θ is 8; when $\Gamma = 0.8$, the number of iteration to find θ is 9. However, the Γ value's effect on the processing time is minor. In this work, Γ is set to be 0.5.

The regulation constant λ is introduced in the vision indicator (Eq. 17) to correctly determine the value of θ . To investigate how λ affects the recovery performance, a recovery quality test was conducted with different values of λ . Fig. 8 shows the results restored via IDGCP from three different types of hazy images with different values of λ when other parameters are fixed at the values listed in Algorithm 1. As shown in the figure, too small λ results in over-saturation in the mist image, whereas too large λ can not completely uncover the scene content in the image with dense haze. As a tradeoff, $\lambda = 0.5$ is selected.

Experiments on numerous sample images demonstrate that once Γ and λ are fixed, the resultant θ values of the images will always lie in a specific confidence interval. When $\Gamma = 0.5$ and $\lambda = 0.5$, the confidence interval is $[0, 6]$. For example, as shown in Fig. 8, the θ values of the three typical images are 0.043, 1.463, and 4.64. More test results can be found on the authors' website¹. Therefore, to reduce the processing time of IDGCP, the initial interval and final interval width used in FM are set to be $[a_1, a_2] = [0, 6]$ and $\varepsilon = 0.1$, respectively.

B. IDGCP Performance Demonstration

1) *Evaluation of IDGCP on different sample images:* First, several sample images were selected from [21] to test the performance of IDGCP. The original sample images, the restored results, and the transmission maps are depicted in Fig. 9 to intuitively demonstrate the capability of IDGCP. As observed in the figure, the proposed IDGCP thoroughly removes the haze and unveils reasonable scene details in hazy regions, while the transmission maps are quite consistent with the objective reality of the real world. Although these estimated transmission maps seem to have a few undesirable or illogical texture details, the visual quality of the recovered results shown in Fig. 9 is already more than sufficient for most cases. Here we remark that further blurring the texture details in transmission maps can improve the restoration quality. However, in this work, the blurring step is omitted as the

¹https://www.researchgate.net/profile/Mingye_Ju



Fig. 9. Image restoration results using the proposed IDGCP.

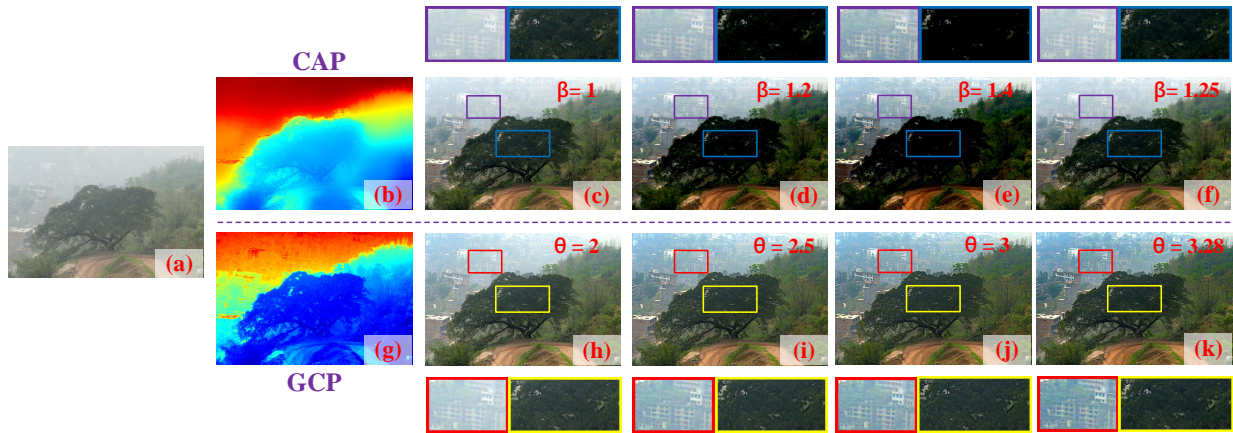


Fig. 10. Comparison of the scene depth obtained by the widely used CAP proposed in [24] and by the proposed GCP. (a): Input hazy image. (b): Depth map obtained via CAP. (c)-(f): Recovered images with different scattering coefficients of $\beta = 1, 1.2, 1.4$, and 1.25 , respectively. $\beta = 1.25$ was determined via the proposed vision indicator. (g): Depth map obtained via GCP. (h)-(k): Recovered images with different constants of $\theta = 2, 2.5, 3$, and 3.28 , respectively. $\theta = 3.28$ was determined via the proposed global optimization strategy.

quality is already satisfactory and the efficiency is the main concern.

2) *Evaluation of the GCP:* The first step of IDGCP is to obtain the depth ratio using GCP. A sharp depth ratio is the premise of the final accurate restoration. In Fig. 10, we compare the obtained scene depth from GCP and that from the widely used color attenuation prior (CAP) [24]. According to the figure, although CAP has a better local-constant feature than GCP (owing to the abandoned blurring step and the ignored locally constant assumption in IDGCP), it is not able to achieve a balance between the over-saturation problem in close-range regions and a complete haze removal in long-range regions by changing the scattering coefficient settings (see the zoom-in patches in Figs. 10(c) to 10(f)). In contrast, GCP is able to solve this problem and achieve satisfactory results by selecting an appropriate value of constant θ (see the zoom-in patches in Fig. 10(k)).

3) *Evaluation of the global-wise strategy:* The pixel-wise, patch-wise, scene-wise, and nonlocal-wise strategies that are designed for haze removal, as aforementioned, involve enormous redundant computations due to the spatial similarity

in natural image. Fig. 11 illustrates the dehazing procedure and the associated time cost of the proposed IDGCP (global-wise) and other recently published works, including FID [15] (pixel-wise), DCP [19] + GF [36] (patch-wise), DIM (scene-wise) [30], and NID (nonlocal-wise) [33]. For fairness of comparison, the redefined scene luminance of DIM was replaced by the atmospheric light, and the atmospheric light of FID, DCP, DIM, NID, and IDGCP were set to have the same value in initialization. As observed in Fig. 11, it is noticed that the transmission maps (or depth maps) estimated via pixel-wise, patch-wise, scene-wise, and nonlocal-wise strategies fail to preserve the edge structure of the original depth or contain many unreasonable texture details, which means that a subsequent refine-transmission step is required. In comparison, IDGCP utilizes the global-wise strategy, which only needs to estimate one unknown constant. This leads to a significant reduction in processing time and computation cost. More importantly, since an entire image has more information than a part of the image, the global-wise strategy can get a more visually comfortable result (as highlighted by red circles in Fig. 11).

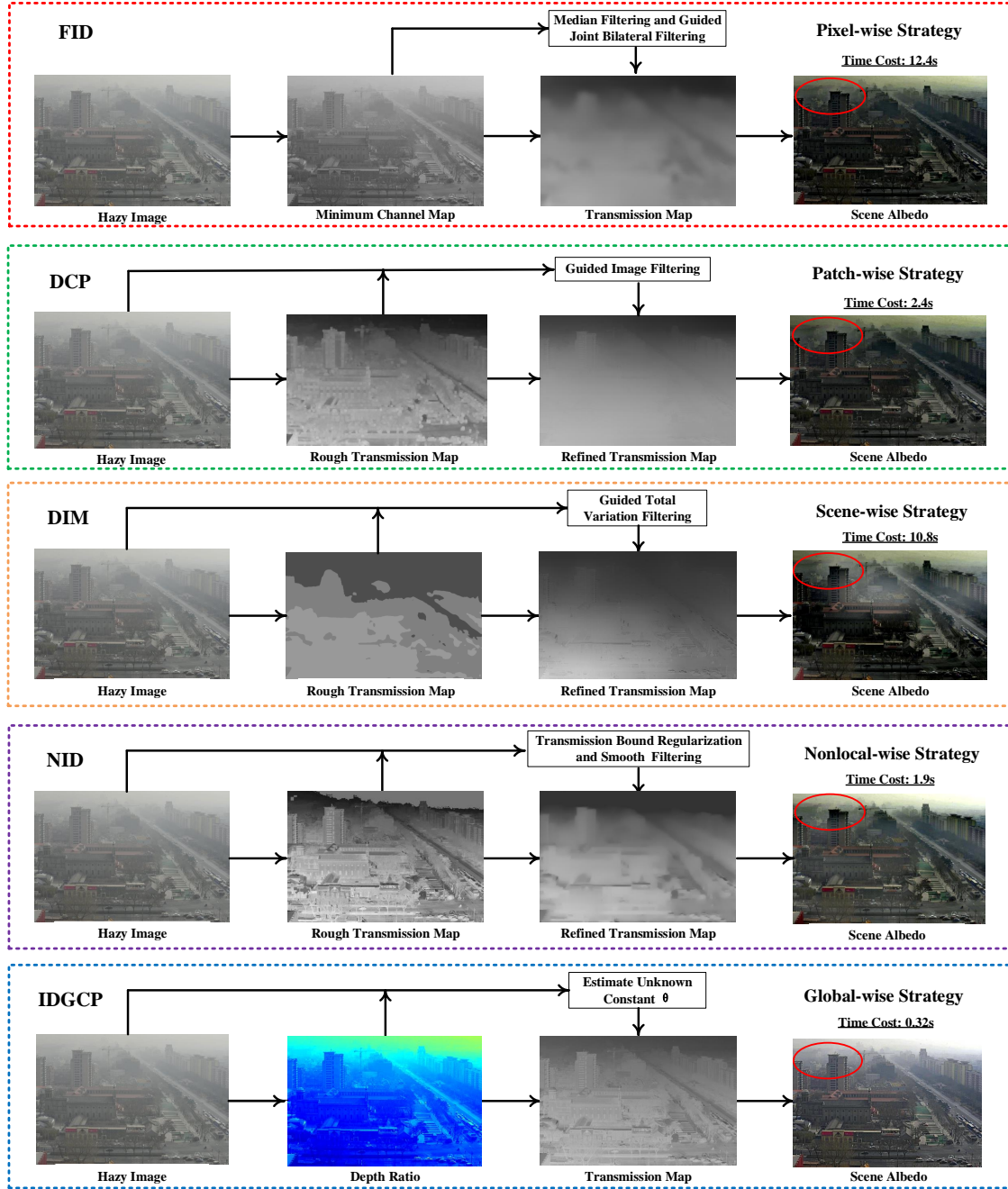


Fig. 11. Overview of image dehazing procedures using FID, DCP + GF, DIM, NID, and the proposed IDGCP. (Note that the atmospheric light is regarded as a known constant here).

C. Qualitative Comparison

1) *Comparison with state-of-the-art dehazing techniques on challenging real-world images:* Almost all the mainstream dehazing techniques are able to get satisfactory restoration results from general outdoor hazy images as discussed in [24], [26]. Sometimes it is hard to tell the differences of the restoration quality using different techniques. In this work, we adopted five widely used challenging real-world benchmark images (collected in [24], [26], [30]) with large white or gray scenes to facilitate the comparison as shown

in Fig. 12. The selected pictures are challenging to dehaze because most of the algorithms are sensitive to the gray-white color. The five hazy images are given in Fig. 12(a). The dehazed results using DEFADE (fusion-wise) [10], FVR (pixel-wise) [13], BCCR (patch-wise) [22], IDAET (scene-wise) [32], IDHL (nonlocal-wise) [34], MSCNN (learning-wise) [27], DehazeNet (learning-wise) [26], and the proposed IDGCP (global-wise) are illustrated in Figs. 12(b) to 12(i), respectively. Some zoom-in detailed are shown in Fig. 12(j) for a clearer comparison.

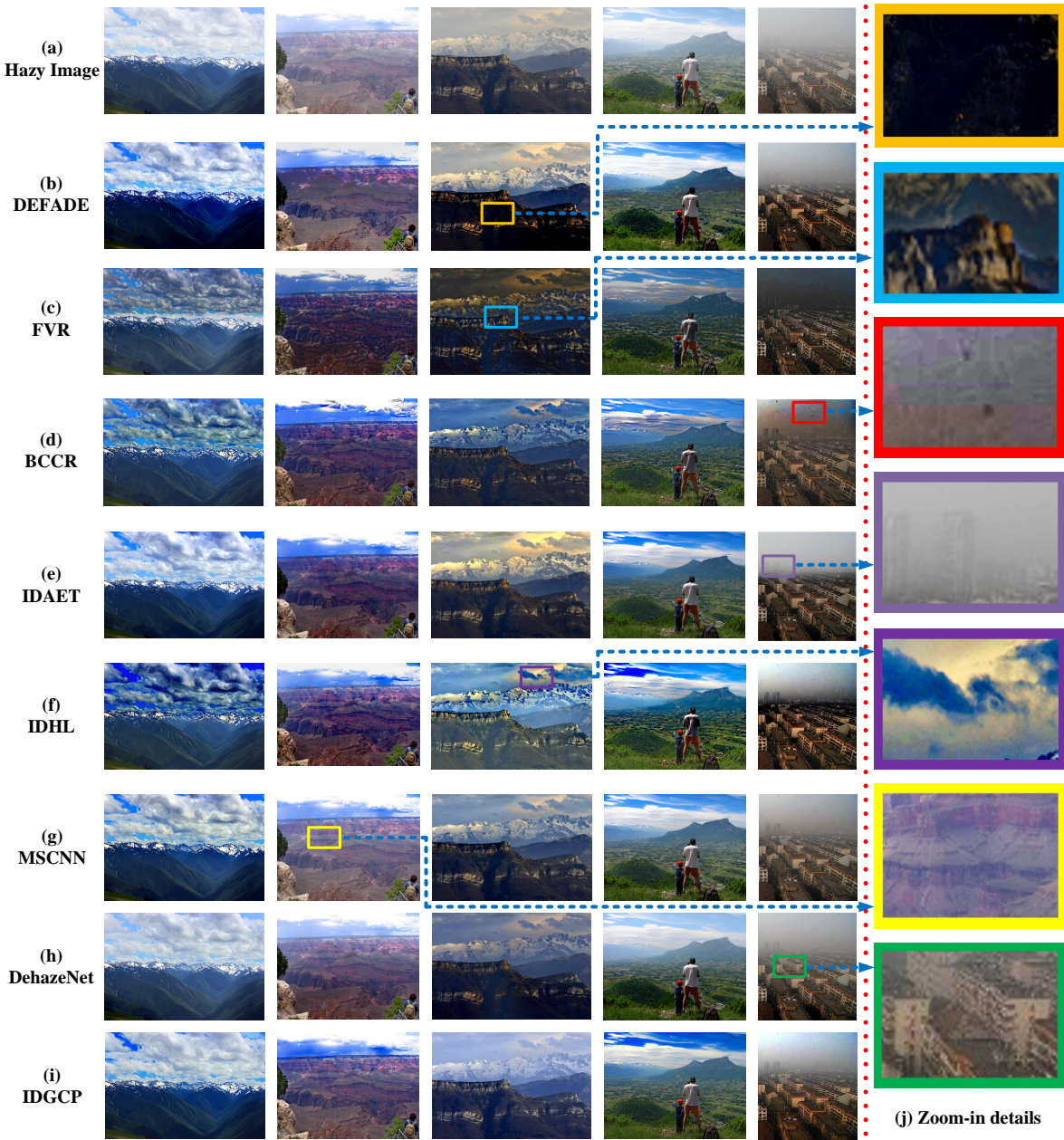


Fig. 12. Qualitative comparison between the proposed IDGCP and other state-of-the-art techniques on five benchmark images.

In Fig. 12(b), it is observed that DEFADE can recognize rough haze regions and increase visual visibility for most of the hazy samples, but its performance is deteriorated when dealing with dark regions (highlighted in the zoom-in subfigure). This is attributed to the fact that the severe dark aspects of the preprocessed images play a dominate role when performing the multi-scale fusion operation. As shown in Fig. 12(c), FVR is able to recover the hidden details of hazy regions, whereas the restoration scenes are quite deviate from the real ones that expected. The reason is that the atmospheric veil used in FVR is a particular case of DCP, and the overestimation transmission problem gets more severe. In addition, for the third picture, halo artifact appears near the depth jumps (see the corresponding zoom-in part in Fig. 12(j)).

This is due to the poor structure-preserving performance of the median filter. Similarly, we notice that BCCR has the same drawback, as shown in Fig. 12(d), because of the fact that the inherent defect of DCP is not addressed and the noise amplification phenomenon still exists in the white regions of the images (as highlighted in Fig. 12(j)). For IDAET as shown in Fig. 12(e), it fails to attain promising results for the dense regions. The reason is that the dense regions are misjudged as “sky” by the transmission compensation module used in this method. IDHL avoids the haze residue for the dense regions by introducing the lower bound of transmission, as seen in Fig. 12(f). However, the over-saturation was unfortunately introduced in recovered result (see the purple patch in Fig. 12(j)). This may be caused by the detection failure of similar

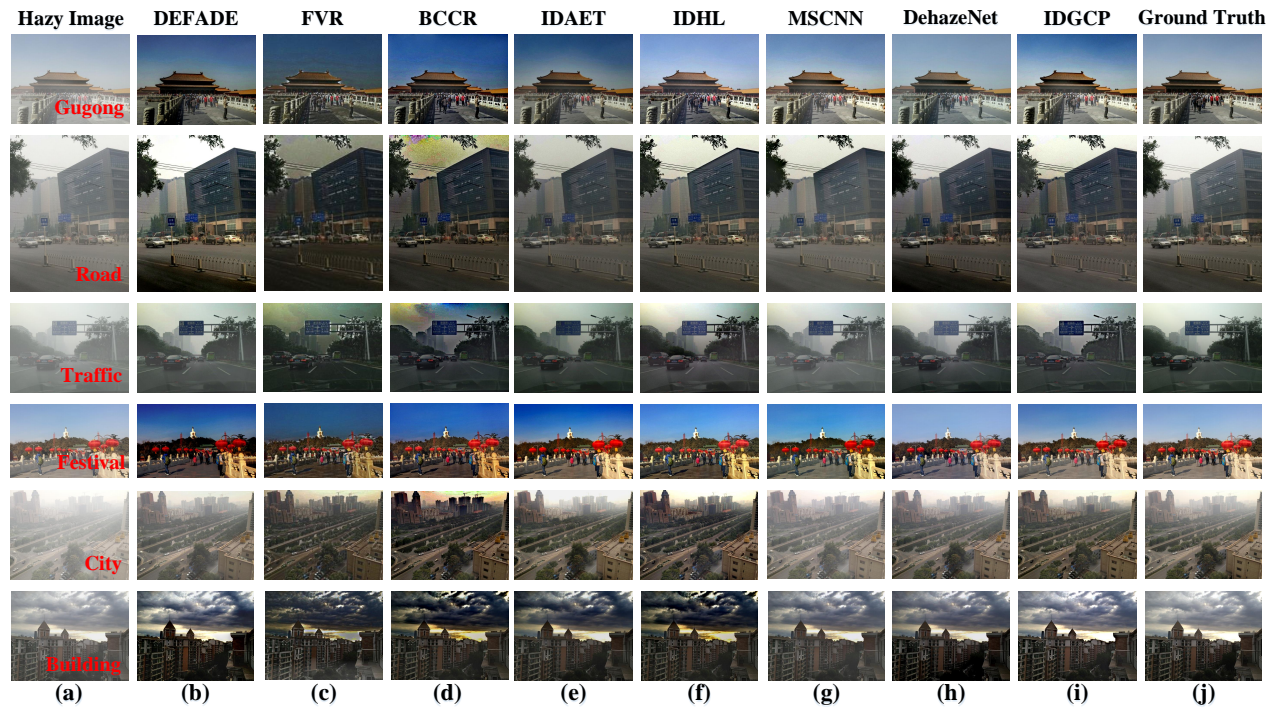


Fig. 13. Qualitative comparison between the proposed IDGCP and other state-of-the-art techniques on synthetic images.

colors. Although MSCNN and DehazeNet can avoid the over-enhancement problem to some extent (see Fig. 12(g) and Fig. 12(h)), haze residue can be found in their dehazed results (detailed in the yellow and green patches). This is mainly attributed to the fact that the training samples for the deep dehazing methods are usually artificially synthesized images rather than real-world images, thus limiting the performance of the learning-wise dehazing methods. Compared with these state-of-the-art techniques, IDGCP is free from over-enhancement, halo effect, and over-saturation problems that degrade the image quality. As displayed in Fig. 12(i), the sky regions and the clouds in the recovery images are very natural, and the texture details of the targets are well enhanced.

2) *Comparison with state-of-the-art dehazing techniques on synthesized images:* Assessing dehazing techniques is a very tricky task since it is difficult to get haze-free reference images from real-world. The comparisons between IDGCP and state-of-the-art techniques were further conducted on the Realistic Single Image Dehazing (RESIDE) dataset [47] consisting of both hazy images and the corresponding haze-free images. Figs. 13(a) and 13(j) give the hazy images and the corresponding ground truth images, respectively. Figs. 13(b) to 13(i) show the recovered results based on the synthesized hazy images using DEFADe, FVR, BCCR, IDAET, IDHL, MSCNN, DehazeNet, and IDGCP, respectively.

In Figs. 13(b) to 13(d), the restored results using DEFADe, FVR, and BCCR can clearly indicate the target contour for the given examples, but their restored colors are generally over-saturated (see the festival image and the building image). As shown in Figs. 13(e) and 13(f), the over-enhancement still exists in the festival images after the dehazing process of IDAET and IDHL. According to Figs. 13(g) and 13(h),

MSCNN and DehazeNet are capable of producing the haze-free results with vivid color and necessary details for mist scenes. However, they lack the ability to uncover the details for the scenes with dense haze (see the city image). In comparison, IDGCP's results do not show any negative effects and can maintain the original tones of most scene targets as shown in Fig. 13(i).

D. Quantitative Comparison on Synthetic Images

In order to guarantee the fairness of the qualitative comparison in Fig. 13, quantitative comparisons were made on four commonly used evaluation indexes. The selected performance indexes are fog aware density evaluator (FADE) [10], edges newly visible after restoration (e) [48], structural similarity (SSIM) [49], and mean square error (MSE). The calculated values of these indexes for the four images shown in Fig. 13 are summarized in Table I. Note that a larger e or a smaller FADE represents a lower perceptual haze density; a larger SSIM means a better structure similarity between the dehazed result and the ground truth image; a lower MSE indicates that the recovered image is more acceptable. It can be concluded from the table that the proposed IDGCP has the highest average value of SSIM and the lowest average value of MSE among all the methods, which means that IDGCP's results are more similar to the ground truth compared with the results obtained by other methods. Although IDGCP has a higher average value of FADE and a lower average value of e than FVR, BCCR, and IDHL, the results produced by these methods appear to be over-saturated and too dark. This could further reduce the perceptual fog density of the dehazed images and increase the pseudo-edge of scene targets.

TABLE I
QUANTITATIVE COMPARISON OF DEHAZED IMAGES SHOWN IN FIG. 13 USING FADE, e , SSIM, AND MSE

Test Criterion	Image	DEFADE	FVR	BCCR	IDAET	IDHL	MSCNN	DehazeNet	IDGCP
FADE	Gugong	0.4201	0.5012	0.3947	0.6571	0.5983	0.7556	1.1620	0.5655
	Road	0.4514	0.6388	0.4344	0.6524	0.5879	0.8593	0.5460	0.5201
	Traffic	1.6470	0.6795	0.7824	1.1191	1.0212	2.1235	1.5703	1.1876
	Festival	0.2656	0.3636	0.3702	0.6231	0.4159	0.5160	0.7604	0.6313
	City	0.9992	0.4355	0.3906	0.6948	0.3916	1.1996	0.8427	0.5231
	Building	0.2592	0.2892	0.3412	0.4891	0.3904	0.7444	0.2901	0.4580
FADE mean value		0.6738	0.5816	0.4522	0.7059	0.5675	1.0331	0.8619	0.6476
e	Gugong	0.4210	0.6115	0.8995	0.4738	0.5727	0.4249	0.4186	0.5208
	Road	1.5946	2.2091	1.8563	1.1783	1.1941	0.6083	1.6055	1.3358
	Traffic	0.6102	1.4777	1.9566	1.7857	1.6927	0.4664	1.4089	1.0192
	Festival	0.2172	0.5007	0.2724	0.1104	0.2033	0.1522	0.0887	0.0455
	City	2.1011	2.8050	3.7393	2.2515	3.5591	1.5653	2.4471	3.4696
	Building	0.6383	0.7569	0.8233	0.5159	0.8672	0.1910	0.2310	0.3393
e mean value		0.9304	1.3935	1.5912	1.0526	1.3482	0.5680	1.0333	1.1217
SSIM	Gugong	0.8396	0.8399	0.8572	0.8451	0.9030	0.9069	0.9474	0.9270
	Road	0.8593	0.8137	0.8548	0.8339	0.9124	0.8941	0.8923	0.9538
	Traffic	0.9097	0.7467	0.8929	0.8658	0.9358	0.8384	0.9615	0.9332
	Festival	0.6828	0.8844	0.9158	0.8934	0.9229	0.8909	0.9829	0.9724
	City	0.3964	0.3292	0.2796	0.3161	0.2712	0.3993	0.3913	0.3713
	Building	0.8357	0.7455	0.8053	0.8305	0.7510	0.8534	0.8543	0.9192
SSIM mean value		0.7539	0.7266	0.7676	0.7641	0.7827	0.7972	0.8383	0.8462
MSE	Gugong	0.0343	0.0345	0.0200	0.0470	0.0088	0.0080	0.0041	0.0072
	Road	0.0084	0.0201	0.0201	0.0197	0.0138	0.0087	0.0106	0.0052
	Traffic	0.0096	0.0517	0.0286	0.0097	0.0090	0.0208	0.0025	0.0061
	Festival	0.0747	0.0199	0.0242	0.0437	0.0163	0.0156	0.0025	0.0036
	City	0.0378	0.0782	0.0654	0.0526	0.0651	0.0479	0.0309	0.0340
	Building	0.0140	0.0335	0.0531	0.0471	0.0535	0.0147	0.0159	0.0083
MSE mean value		0.0298	0.0397	0.0352	0.0366	0.0278	0.0193	0.0111	0.0107

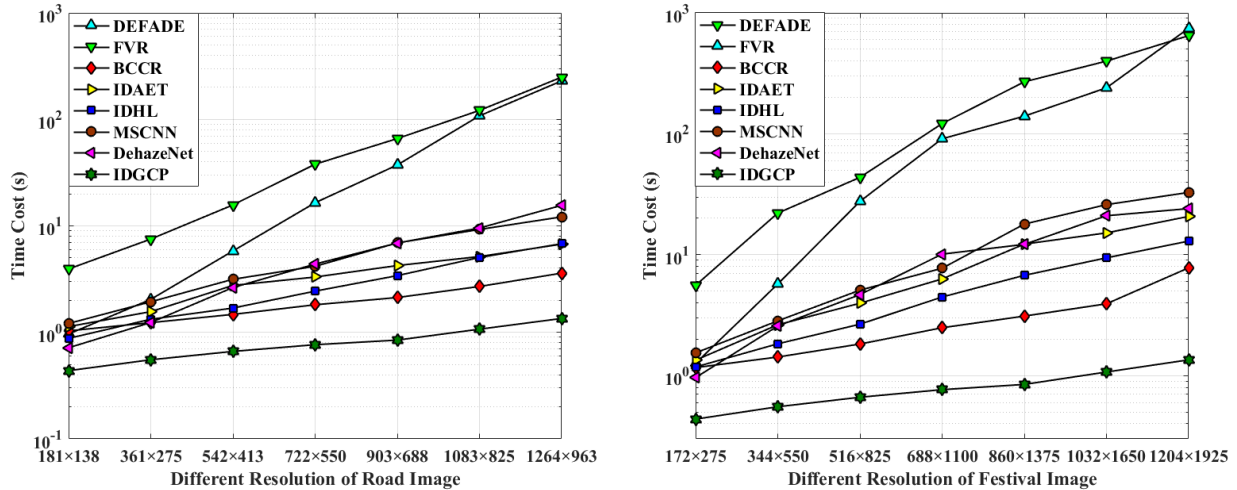


Fig. 14. Comparison of the processing time of dehazing two example images with tunable resolutions using the proposed IDGCP and other state-of-the-art techniques.

E. Comparison of the Processing Time

Except the high restoration quality, the most significant advantage of the proposed IDGCP is the low computation complexity thus reducing processing time. Eqs. 7, 12, 14 and the quad-tree subdivision method [14] used in IDGCP are all simple operations, and the main calculation cost of IDGCP is the gradient operation to determine the unknown constant θ (see Eq. 15 and Eq. 17). Therefore, given an image of size $l \times w$, the theoretical complexity of IDGCP is only $\mathcal{O}(\frac{100 \cdot l \cdot w}{\max(w, l)})$. To demonstrate the efficiency of IDGCP, a comparison of the processing time between different techniques

dealing with images with different resolutions is shown in Fig. 14. To ensure the fairness of the comparison, two pictures (the "road" and "festival" images shown in Fig. 13) with tunable resolutions were used in comparison and all the tests were performed five times to get the average time cost. It can be easily concluded from Fig. 14 that IDGCP is significantly faster than all the other techniques regardless of the resolution of the images.

Overall, the comparison results shown in Figs. 9 to 14 and Table I demonstrate that the proposed IDGCP outperforms most of the state-of-the-art methods in terms of haze removal, color restoration, and processing time while avoiding almost

all of the negative effects.

VI. CONCLUSION

In this paper, a very simple yet powerful gamma correction prior (GCP) was proposed, leading to an extremely efficient single image dehazing method called IDGCP. The proposed GCP allows us to approximately simulate a homogeneous misty image from an input hazy image. Based on this prior and atmospheric scattering model, IDGCP was developed. Unlike previous works, IDGCP converts single image dehazing into multiple images haze removal task. The benefit is to ease the uncertainty of depth information, so that the haze removal task can be redefined as a global-wise optimization function to determine only one unknown constant. IDGCP can obtain a high-quality transmission map without any refining process, which significantly reduces the processing time. A series of experimental results demonstrate that IDGCP achieves noticeably higher efficiency and outstanding dehazing ability compared to the state-of-the-art techniques.

REFERENCES

- [1] J. Redmon, S. Divvala, R. Girshick, and A. Farhadi, "You only look once: Unified, real-time object detection," in *Proc. 2016 IEEE Conf. Comput. Vis. Pattern Recognit.*, Jun. 2016, pp. 779–788.
- [2] G. Woodell, D. J. Jobson, Z. Rahman, and G. Hines, "Advanced image processing of aerial imagery," in *Proc. SPIE, Vis. Inf. Process. XV*, 2006, vol. 6246, pp. 1–12.
- [3] J. Z. Wang, W. M. Wang, R. G. WANG, W. GAO, "CSPS: an adaptive pooling method for image classification," *IEEE Trans. Multimedia*, vol. 18, no. 6, pp. 1000–1010, Jun. 2016.
- [4] T. K. Kim, J. K. Paik, and B. S. Kang, "Contrast enhancement system using spatially adaptive histogram equalization with temporal filtering," *IEEE Trans. Consum. Electr.*, vol. 44, no. 1, pp. 82–87, Mar. 1998.
- [5] T. J. Cooper and F. A. Baqai, "Analysis and extensions of the Frankle-McCann Retinex algorithm," *J. Electron. Imaging*, vol. 13, no. 1, pp. 85–92, 2004.
- [6] M. J. Seow and V. K. Asari, "Ratio rule and homomorphic filter for enhancement of digital colour image," *Neurocomputing*, vol. 69, no. 7–9, pp. 954–958, 2006.
- [7] G. Deng, L. W. Cahill, and G. R. Tobin, "The study of logarithmic image processing model and its application to image enhancement," *IEEE Trans. Image Process.*, vol. 4, no. 4, pp. 506–512, May. 1995.
- [8] A. Polesel, G. Ramponi, and V. J. Mathews, "Image enhancement via adaptive unsharp masking," *IEEE Trans. Image Process.*, vol. 9, no. 3, pp. 505–510, Feb. 2000.
- [9] C. O. Ancuti and C. Ancuti, "Single image dehazing by multi-scale fusion," *IEEE Trans. Image Process.*, vol. 22, no. 8, pp. 3271–3282, May 2013.
- [10] L. K. Choi, J. You, and A. C. Bovik, "Referenceless prediction of perceptual fog density and perceptual image defogging," *IEEE Trans. Image Process.*, vol. 24, no. 11, pp. 3888–3901, Jul. 2015.
- [11] S. G. Narasimhan and S. K. Nayar, "Contrast restoration of weather degraded images," *IEEE Trans. Pattern Anal. Mach. Intell.*, vol. 25, no. 6, pp. 713–724, Jun. 2003.
- [12] J. Kopf, B. Neubert, B. Chen, and D. Lischinski, "Deep photo: Model-based photograph enhancement and viewing," *ACM Trans. Graphics.*, vol. 27, no. 5, pp. 1–10, 2008.
- [13] J. P. Tarel and N. Hautiere, "Fast visibility restoration from a single color or gray level image," in *Proc. 2009 IEEE 12th Int. Conf. Comput. Vis.*, Oct. 2009, pp. 2201–2208.
- [14] W. C. Wang, X. H. Yuan, X. J. Wu, and Y. L. Liu, "Fast image dehazing method based on linear transformation," *IEEE Trans. Multimedia*, vol. 19, no. 6, pp. 1142–1155, Jan. 2017.
- [15] C. X. Xiao and J. J. Gan, "Fast image dehazing using guided joint bilateral filter," *Visual Comput.*, vol. 28, no. 6–8, pp. 713–721, 2012.
- [16] M. Y. Ju, C. Ding, D. Y. Zhang, and Y. J. Guo, "BDPK: Bayesian Dehazing Using Prior Knowledge," *IEEE Trans. on Circuits and Systems for Video Technology*, vol. 29, no. 8, pp. 2349–2362, Jan. 2018.
- [17] M. Y. Ju, C. Ding, D. Y. Zhang, and Y. J. Guo, "Gamma-Correction-Based Visibility Restoration for Single Hazy Images," *IEEE Signal Processing Letters.*, vol. 25, no. 7, pp. 1084–1088, 2018.
- [18] M. Y. Ju, Z. F. Zhang, and Y. Deng, "Single image haze removal based on the improved atmospheric scattering model," *Neurocomputing*, vol. 260, pp. 180–191, 2017.
- [19] K. M. He, J. Sun, and X. O. Tang, "Single image haze removal using dark channel prior," *IEEE Trans. Pattern Anal. Mach. Intell.*, vol. 33, no. 12, pp. 2341–2353, Sept. 2011.
- [20] T. M. Bui, and W. Kim, "Single Image Dehazing Using Color Ellipsoid Prior," *IEEE Trans. Image Process.*, vol. 27, no. 2, pp. 999–1009, Feb. 2018.
- [21] R. Fattal, "Dehazing using color lines," *ACM Trans. Graphics.*, vol. 34, no. 1, pp. 1–14, 2014.
- [22] G. F. Meng, Y. Wang, J. Y. Duan, S. M. Xiang, and C. H. Pan, "Efficient image dehazing with boundary constraint and contextual regularization," in *Proc. 2013 IEEE Int. Conf. Comput. Vis.*, Dec. 2013, pp. 617–624.
- [23] S. C. Huang, J. H. Ye, and B. H. Chen, "An advanced single-image visibility restoration algorithm for real-world hazy scenes," *IEEE Trans. Ind. Electron.*, vol. 62, no. 5, pp. 2962–2972, May 2015.
- [24] Q. S. Zhu, J. M. Mai, and L. Shao, "A fast single image haze removal algorithm using color attenuation prior," *IEEE Trans. Image Process.*, vol. 24, no. 11, pp. 3522–3533, Jun. 2015.
- [25] L. Y. He, J. Z. Zhao, N. N. Zheng, and D. Y. Bi, "Haze removal using the difference-structure-preservation prior," *IEEE Trans. Image Process.*, vol. 26, no. 3, pp. 1063–1075, Dec. 2017.
- [26] B. L. Cai, X. M. Xu, K. Jia, C. M. Qing, and D. C. Tao, "Dehazenet: An end-to-end system for single image haze removal," *IEEE Trans. Image Process.*, vol. 25, no. 11, pp. 5187–5198, Aug. 2016.
- [27] W. Q. Ren, S. Liu, H. Zhang, J. S. Pan, X. C. Cao, and M.-H. Yang, "Single Image Dehazing via Multi-Scale Convolutional Neural Networks," *European Conference on Computer Vision (ECCV)*, pp. 154–169, 2016.
- [28] B. Li, X. Peng, Z. Wang, J. Xu, and D. Feng, "Aod-Net: all in one dehazing network," *IEEE International Conference on Computer Vision (ICCV)*, pp. 4770–4778, 2017.
- [29] K. Tang, J. C. Yang, and J. Wang, "Investigating haze-relevant features in a learning framework for image dehazing," in *Proc. 2014 IEEE Conf. Comput. Vis. Pattern Recognit.*, Jun. 2014, pp. 2995–3002.
- [30] M. Y. Ju, D. Y. Zhang, and X. M. Wang, "Single image dehazing via an improved atmospheric scattering model," *Visual Comput.*, vol. 33, no. 12, pp. 1613–1625, 2017.
- [31] H. Yuan, C. C. Liu, Z. X. Guo, and Z. Z. Sun, "A region-wised medium transmission based image dehazing method," *IEEE Access*, vol. 5, pp. 1735–1742, Jan. 2017.
- [32] G. L. Bi, J. Y. Ren, T. J. Fu, T. Nie, C. Z. Chen, N. Zhang, "Image Dehazing Based on Accurate Estimation of Transmission in the Atmospheric Scattering Model," *IEEE Photonics Journal*, vol. 9, no. 4, pp. 1–18, Aug. 2017.
- [33] D. Berman, T. Treibitz, and S. Avidan, "Non-local Image Dehazing," in *2016 IEEE Conference on Computer Vision and Pattern Recognition (CVPR)*, 2016, pp. 1674–1682.
- [34] D. Berman, T. Treibitz and S. Avidan, "Single Image Dehazing Using Haze-Lines," *IEEE Trans. Pattern Anal. Mach. Intell.*, Early Access.
- [35] Y. Bahat and M. Irani, "Blind dehazing using internal patch recurrence," in *Proc. 2016 IEEE International Conference on Computational Photography*, May. 2016, pp. 1–9.
- [36] K. He, J. Sun, and X. Tang, "Guided image filtering," *IEEE Trans. Pattern Anal. Mach. Intell.*, vol. 35, no. 6, pp. 1397–1409, Jun. 2013.
- [37] A. Levin, D. Lischinski, and Y. Weiss, "A closed-form solution to natural image matting," *IEEE Trans. Pattern Anal. Mach. Intell.*, vol. 30, no. 2, pp. 228–242, Mar. 2008.
- [38] C. X. Liu, J. W. Zhao, Y. Y. Shen, Y. G. Zhou, X. Wang, and Y. Ouyang, "Texture filtering based physically plausible image dehazing," *Visual Comput.*, vol. 32, no. 6–8, pp. 911–920, 2016.
- [39] X. Dong, G. Wang, Y. Pang, W. X. Li, J. T. Wen, W. Meng, and Y. Lu, "Fast efficient algorithm for enhancement of low lighting video," in *Proc. 2011 IEEE Int. Conf. Multimedia Expo*, Jul. 2011, pp. 1–6.
- [40] L. Li, R. G. Wang, W. M. Wang, and W. Gao, "A low-light image enhancement method for both denoising and contrast enlarging," in *Proc. 2015 IEEE Int. Conf. Image Process.*, Sept. 2015, 3730–3734.
- [41] X. J. Guo, Y. Li, and H. B. Ling, "LIME: Low-light image enhancement via illumination map estimation," *IEEE Trans. Image Process.*, vol. 26, no. 2, pp. 982–993, Feb. 2017.
- [42] R. T. Tan, "Visibility in bad weather from a single image," in *Proc. 2008 IEEE Conf. Comput. Vis. Pattern Recognit.*, Jun. 2008, pp. 1–8.

- [43] J. H. Kim, W. D. Jang, J. Y. Sim, and C. S. Kim, "Optimized contrast enhancement for real-time image and video dehazing," *J. Vis. Commun. Image R.*, vol. 24, no. 3, pp. 410–425, 2013.
- [44] D. Scharstein and R. Szeliski, "A taxonomy and evaluation of dense two-frame stereo correspondence algorithms," *Int. J. Comput. Vis.*, vol. 47, no. 1–3, pp. 7–42, 2002.
- [45] D. Scharstein and R. Szeliski, "High-accuracy stereo depth maps using structured light," in *Proc. 2003 IEEE Comput. Soc. Conf. Comput. Vis. Pattern Recognit.*, Jun. 2003, vol. 1, pp. 195–202.
- [46] D. Scharstein and C. Pal, "Learning conditional random fields for stereo," in *Proc. 2007 IEEE Conf. Comput. Vis. Pattern Recognit.*, Jun. 2007, pp. 1–8.
- [47] B. Li, W. Ren, D. Fu, D. Tao, D. Feng, W. Zeng, and Z. Wang, "Benchmarking Single-Image Dehazing and Beyond," *IEEE Trans. Image Process.*, vol. 28, no. 1, pp. 492–505, 2019.
- [48] N. Hautière, J. P. Tarel, D. Aubert, and E. Dumont, "Blind contrast enhancement assessment by gradient ratioing at visible edges," *Image Anal. Stereol.*, vol. 27, no. 2, pp. 87–95, 2011.
- [49] Z. Wang, A. C. Bovik, H. R. Sheikh, and E. P. Simoncelli, "Image quality assessment: From error visibility to structural similarity," *IEEE Trans. Image Process.*, vol. 13, no. 4, pp. 600–612, Apr. 2004.